EUROFUSION WPPFC-PR(16) 16405

C Pardanaud et al.

Preparing the future post-mortem analysis of Beryllium-based JET and ITER samples by means of multi-wavelengths Raman spectroscopy

Preprint of Paper to be submitted for publication in
Nuclear Fusion

This work has been carried out within the framework of the EUROfusion Consortium and has received funding from the Euratom research and training programme 2014-2018 under grant agreement No 633053. The views and opinions expressed herein do not necessarily reflect those of the European Commission.

Preparing the future *post-mortem* analysis of Beryllium-based JET and ITER samples by means of multi-wavelengths Raman spectroscopy

M. I. Rusu[a,b], C. Pardanaud[b*], C. Martin[b], Y. Addab[b], P. Roubin[b], Y. Ferro[b], M. Minissale[b], L. Ferry[b,c], F. Virot[c], M. Barrachin [c], C P Lungu[d], C Porosnicu[d], P Dinca[d], M Lungu[d], M. Köppen[e], P. Dollase[e], Ch. Linsmeier[e]

[a]*National Institute of R&D for Optoelectronics INOE 2000, Ilfov, Romania*

[b] *Aix Marseille Univ, CNRS, PIIM, Marseille, France*

[c] *Institut de Radioprotection et Sûreté Nucléaire, B.P. 3, 13115 Saint Paul-lez-Durance Cedex, France*

[d]*National Institute for Laser, Plasma and Radiation Physics, 077125, Magurele-Bucharest, Romania*

[e] *Forschungszentrum Jülich GmbH, Institut für Energie- und Klimaforschung - Plasmaphysik, 52425 Jülich, Germany*

[*]Corresponding author: cedric.pardanaud@univ-amu.fr

Abstract

This study demonstrates that Raman microscopy is a suitable technique for future *post mortem* analyses of JET and ITER PFCs. We focus here on Laboratory deposited and bombarded samples of beryllium and beryllium carbides *and start to build reference spectral databases for beryllium-based samples.* We identified the beryllium Phonon Density of State, its second harmonic and E_{2G} and B_{2G} second harmonic and combination modes for defective beryllium in the spectral range 300-700 and 700-1300 cm^{-1}, lying close to Be-D modes of beryllium hydrides or to Be-O modes of beryllium oxide. We also identified beryllium carbide signature, Be_2C, combining Raman microscopy and DFT calculation. *In-depth analysis at the nanometric scale can also be performed with different laser wavelengths.* This way, we demonstrate that multi-wavelength Raman microscopy is sensitive to in-depth stress caused by ionic implantation (down to 30 nm under the surface for Be) and Be/C concentration (down to 400 nm under the surface for Be+C), which is a main contribution of this work. The depth resolution reached is then adapted for studying the supersaturated surface layer found on tokamak deposits.

I. Introduction

The aim of this work is to demonstrate that Raman microscopy is a well-suited technique for the post-mortem analysis of the future ITER and JET walls. Using different Laboratory samples, we herein set-up the basis of an experimental methodology in order for Raman microscopy to be used as a characterization technique.

Being able to predict the evolution of the plasma facing components (PFCs) that interact with both heat loads and the edge plasma is one of the keystones to make nuclear fusion a way of producing energy in the future [1]. The PFC of the future international reactor ITER that will receive most of the particle flux and/or heat loads is the tungsten divertor, while the other PFCs will be composed of beryllium [2]. Some tokamaks are already working nowadays in an ITER-Like-Wall (ILW) configuration in order to prepare the ITER project, such as the Joint European Torus/JET tokamak in which some PFCs are composed of tungsten coated carbon tiles [3-5]. Carbon tiles were used in the ancient carbon area of tokamaks but are now abandoned to limit tritium retention [6, 7]; they nevertheless remain a source of carbon contamination for beryllium and tungsten materials. In that framework, the surface composition and morphology modifications under operation will lead to changes in the material properties, some of them related to safety issues; these changes will have to be measured and understood. The lifetime of these PFCs and their fuel retention properties will be influenced by the migration [8] and/or melting of elements in the machine [9, 10], the production of dust, the hydrogen isotope retention [11, 12], the complex surface erosion mechanisms, and the impurity contamination (traces of carbon and/or oxygen, nitrogen seeding [13],...) leading to formation of new mixed materials/phases. Surface characterisation techniques are then necessary to measure the elemental changes in JET and in ITER.

Due to their isotope selectivity, Ion Beam Analyses (IBA) play a prominent role in this characterization, as discussed in [14, 15]. Thermal Desorption Spectroscopy (TDS) also plays a role as it gives access to the characterization of D or T trapping energies in metals such as Be [16-18] or W [19]. These trapping energies are usually compared with those calculated by Density Functional Theory (DFT) [20] [21] or incorporated in Rate-Equation modellings that fit the experimental TDS spectra [22]. However, even if TDS and IBA techniques give quantitative information about hydrogen isotope concentration, they only give indirect information about chemical bonding. A direct way to probe the chemical environment is to probe it spectroscopically by means of its vibrational spectrum using Raman microscopy. The vibrational frequencies can also be computed by DFT, which complemented the Raman analysis. Raman microscopy is a nondestructive, non contact, and local ($\approx 1 \mu m^2$ lateral resolution [23]) technique that has been proved to be sensitive to Be stretching modes [24], beryllium oxide modes [25], bending and stretching tungsten oxide modes [26], Be_xW_y mixed samples density of states [27], BeCW irradiated samples [28], and give information when a pristine

material is implanted by hydrogen ions [27, 29, 30]. First Raman analyses in ILW-tokamaks were performed on some molybdenum JET mirrors [27], showing that the technique is sensitive to thin ≈10 nm deposited layer composed of ≈33% Be, ≈33% C and ≈33% O and the underlying molybdenum oxidized mirror. C-O and C=O modes have been detected in that layer, and defective or beryllium mixed with O and/or C have been found without possibility to identify the phases rigorously up to now, because of a poor benchmarking of the technique for these materials. Raman microscopy can also be able to give information about the hydrogen isotope behavior, by combining IBA, Raman microscopy, Atomic Force Microscopy (AFM) and with the help of DFT modeling. As an illustration of this complementarity, in [31], we identified on laboratory experiments the growth of BeD_2 with dendritic forms appearing subsequently to 2 keV ion implantation when the Be layer is saturated by implanted D ions. The width of the bands recorded by Raman microscopy suggested that this hydride has grown in a crystalline form which seems to be close to a body centered orthorombic structure with I_{bam} symmetry as the spectra look like to the ones reported in [32], who determined recently the structure by using additionally synchrotron X-ray diffraction. In [31], we showed that these dendrites appear when the amount of deuterium in the material is higher than ≈2 10^{17}D.cm^{-2}, when the ≈40 nm under surface layer is saturated by D.

The paper is organized as follow. In part 2, we present the experimental and theoretical methods. In part 3 we present the results that are divided in four subparts: part a and b are devoted to the analysis of defective beryllium samples, respectively obtained by deposits and by implanting deuterium using two implantation geometries, and part c is devoted to the analysis of beryllium carbides. Part d put all the results together to better highlight the spectroscopic parameters that matter. In part 4, we discuss the results and give a conclusion in part 5.

II. Methods

II. 1 Sample preparation

As the aim of this work is to demonstrate that Raman microscopy is a well-suited technique for the post-mortem analysis of the future ITER and JET walls, using different Laboratory samples, we produced tokamak-like samples which are deposits and implanted samples. In deposits, we varied the amount of defects to study the corresponding Raman signature.

Depositions of 400 nm thick Be and co deposited Be+C layers were performed on silicon substrates using the thermionic vacuum (TVA) method for which the emission of an electron beam produced by a heated filament is focused using a special Wehnelt device toward an anode connected to a high voltage regulated power supply. More details can be found in [33] and references therein. The TVA plasma spatial localization allows gas injection close to the substrate during the deposition. Three Be samples were synthesized with different amount of defects (referred as sample 1, 2 and 3).

We used partial pressure of N_2 and D_2 (in the range 10^{-2} to 10^{-3} Pa partial pressure) to introduce this disorder, the amount of N and D being respectively 3-8 atomic % for sample 1, <0.4 atomic % for sample 2 and no additional gas injection for sample 3 [27]. Then sample 1 contains more defects than sample 2, which itself contains more defects than sample 3. For beryllium carbide samples, partial pressure of the Be/C in the substrate vicinity was also in the same range. We used two ratios: Be/C=0.3 and 1.

The D-implanted Be samples are prepared in a multi-chamber XPS system by PREVAC under UHV conditions with a base pressure in the low 10^{-10} hPa range. The system is equipped with a MX-650 monochromatic X-ray source and a R4000 hemispherical energy analyser, both from VG Scienta. In addition, a UV source type PREVAC UVS 40A2 is attached. Sputter cleaning and implantations are performed by a PREVAC 40E1 ion source. All sample preparation steps are performed in-situ without breaking the vacuum. The Be-samples, from MaTecK, have a size of 10 x 10mm² and an average surface roughness of R_a<1 µm. The samples are cyclically cleaned by Ar^+ ion sputtering with 3 keV for 30 min and annealing at 600 °C for 45 minutes, until no surface contaminations are visible in the XP-spectra. Both samples have an implantation area of 3 x 3 mm². The Beryllium samples is implanted with a fluency of 38.4D-atoms per Å². For the fluency calculation a beam composition of 2 % D^+ and 98 % D_2^+ is assumed. [1] The XP spectra show no surface contaminations but oxygen.

II. 2 Computational details

The calculations in this work are based on DFT as implemented in the Quantum Espresso Package [34].The Perdew-Burke-Ernzerhof functional (PBE) [35] built in the generalized gradient approximation (GGA) is used to compute the exchange and correlation energies. The same ultra-soft pseudopotentials [36] (USPPs) as in [37, 38] were used to model the ionic cores.

We used energy cutoffs of 40 Ry and 320 Ry for the truncation of the plane-wave expansion of the wave function and the electronic density, respectively. The Brioullin zone is sampled in a 14 ×14 ×14 grid of k points. Beryllium carbide Be_2C crystallized with C atoms in a face centered cubic structure *fcc* and Be atoms occupying all the tetrahedral sites available in Fluorite CaF_2 type a structure. The working-cell contains four carbon and twelve beryllium atoms. The calculated cell parameter **a**=4.310 Å is found in good agreement with the experimental one $\mathbf{a_{exp}}$= 4.342 Å.

II. 3 Sample characterization

For Be samples (referred as sample 1, 2 and 3) X-ray diffraction was performed, and size domains were deduced. Using the Be(100) diffraction peak, the crystallite sizes of sample *1*, *2* and *3* are respectively 34.0(4.5) nm, 25.0(2.9) nm and 19.0(1.9) nm. Only sample *1* gives Be(002) and Be(101) diffraction peaks, the crystallite sizes deduced being respectively 27.8(4.4) nm and 34.6(5.2)

nm, the three sizes being identical taking into account the error bars. The size of the crystallites for the reference material is more than 10 μm, and we consider it as infinite compared to the one of sample *1*, *2* and *3*.

Raman spectra were recorded on all the samples using a Horiba-Jobin-Yvon HR LabRAM apparatus in the backscattering geometry (with x100 objective, with a numerical aperture of 0.9 for. λ_L = 488, 514.5 and 632.8 nm, and x40 for λ_L=325 nm). The Raman mapping mode was also used, and sometimes necessary to increase the signal to noise ratio. The laser power was kept at ~ 1mW μm^{-2}. For safety reasons, we simulated the influence of the power laser on a beryllium sample in air and deposited on a silicon wafer, by taking into account geometric effects, heat diffusion in materials and convection in air, by means of the COMSOL software. The main trend is that working with this power density is safe, but more details of the modeling are given in appendix.

II. 4 Sensitivity/capabilities of Raman microscopy

A review of all the capabilities of this technique can be found in [23]. In this part we only give the main ideas in term of sensitivity and spectral windows of relevant materials useful for plasma wall interaction in tokamaks studies. Figure 1 displays Raman spectra of such materials. They have been acquired in the same experimental conditions, using the same experimental set-up, to allow comparison of their intensities and to give a concrete idea on which materials can be measured easily or not and under which experimental conditions. One has to note that this plot does not give directly the Raman cross sections, as to determine them it should be necessary to take into account the geometry of the set up used, the optical constants of the materials and to calibrate the detector, which is not under the scope of this work. The wavelength used here is λ_L=514 nm, the objective is a 100x with numerical aperture of 0.9, grating is 600 grooves per mm and we used backscattering geometry.

The conditions of acquisition known to give very intense Raman spectra were 60 seconds of integration without averaging on silicon, graphite and 200 nm thick hydrogenated amorphous carbon [39] ?? For tungsten oxide, graphene (one layer on top of silicon) and beryllium, the acquisition time was also 60 seconds but averaged 150 times in order to increase the signal to noise ratio. For BeD_2, an average of ≈250 spectra was necessary.

The main features appearing in Figure 1 are:

- In silicon crystal, the phonon mode at 520 cm^{-1} is known to give a very intense Raman band that we use here for comparison (it is also used as a wafer for the Be+C codeposits). Features in the Raman spectrum at 300, 640 and 950 cm^{-1}, and roughly one to two orders of

magnitudes less intense than the 520 cm^{-1} band, are due to combination modes and overtones [40-42].

- In 200 nm thick hydrogenated amorphous carbon (a-C:H) the well known D and G broad bands rise, corresponding to aromatic carbons that can give information on the defects, nanometric clustering of the material and the hydrogen content (see [43] and references there in).
- In graphite, the stretching mode of C-C bonds is known to give only one Raman band lying at 1582 cm^{-1} in the 1000-1800 cm^{-1} spectral window [44]. This band is less intense than that of the a-C:H, due to differences existing in optical constants (i. e. graphite absorbs more than a-C:H [45]). Note that the full width at half maximum (noted hereafter Γ) of the bands related to a-C:H are higher by an order of magnitude than that of graphite, then one can estimate the degree of disorder, as it is discussed in [46].
- In 200 nm thick tungsten oxide layer grown under O_2 atmosphere at 400°C on top of tungsten (see [30] for more details), is one order of magnitude lower than silicon. It is roughly composed of two broad bumps, below and above 500 cm^{-1}. The last one is composed of three overlapping bands lying at approximately 700, 800 and 960 cm^{-1}. The first and second ones are due respectively to transverse and longitudinal optical phonons, and the shoulder at 960 cm^{-1} is attributed to W=O terminal bonds (see [47] and references therein for more details).
- In beryllium, the stretching mode of Be-Be bonds (E_{2G} symmetry[1]) is known to give only one Raman band lying at σ_{Be}= 450 cm^{-1} in the 100-1100 cm^{-1} spectral window, the other one (B_{2G} being infrared active). Broad bands lying at 645, 887 and between 1008 and 1113 cm^{-1} have been attributed to defect induced bands in [27]. We will investigate it deeper when describing figure 3.
- BeD_2 gives 4 groups of bands, close to 270, 615, 909 and 1710 cm^{-1}, as it was shown in [31] and more recently in [32], where 3 groups of bands were found. The 270, 615 and 909 cm^{-1} groups may be due to a BeD_2 close to a body centered orthorhombic structure with I_{bam} symmetry whereas the 1710 cm^{-1} could be related to surface modes, as the surface to volume ratio is high, as shown by atomic force microscopy [31]. The intensity of these bands is roughly a factor of two lower than the intensity corresponding to the 1580 cm^{-1} band of a graphene layer. If we take into account the volume probed, (100-200 nm height for the dendrites evidenced in [31]) then the Raman cross section is estimated to be roughly 300 times smaller in the case of BeD_2 than in the case of graphene.

[1] Symmetry of a crystal atomic structure can be described by symmetry operations forming group space. Mode symmetry at the gamma point of the Brilliouin zone, deduced from the point group symmetry of the given crystal, allow to determine if a mode will be Raman active or not.

Most of these spectroscopic parameters/features will be used in order to assess and determine defects and impurities in beryllium based materials.

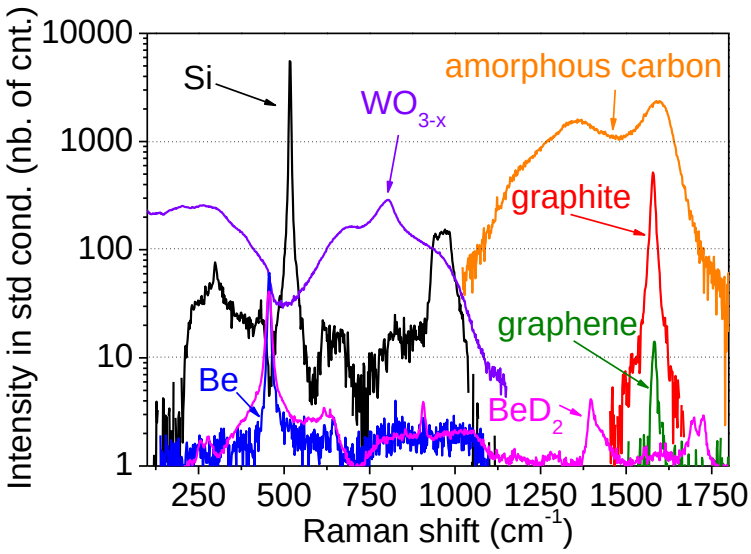

Figure 1. *Raman spectra of materials relevant for plasma wall interactions with standard acquisition conditions. See the text for details. Silicon is used as a reference.* λ_L*=514 nm.*

III. Results

III. 1 Nanocrystalline Be deposits

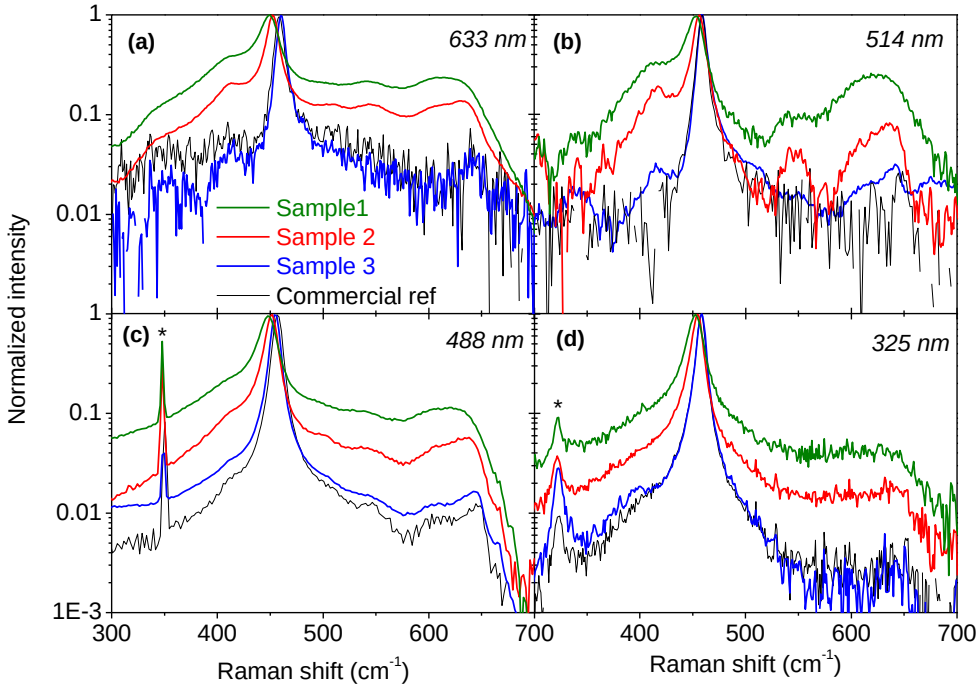

Figure 2*. Normalized Raman spectra of deposited samples 1, 2 and 3 compared to commercial Be microcrystal, for four wavelengths laser excitation wavelength: (a) 633 nm, (b) 514 nm, (c) 488 nm and (d) 325 nm. The bands marked by stars are due to other laser electronic transitions.*

Figure 2 displays Raman spectra of deposited Be samples 1, 2 and 3 plus the commercial reference sample for 4 laser wavelengths. We focus first on the 633 nm data (Fig. 3-a). The band associated to the E_{2G} Raman active mode is down shifted for sample 1 and 2 whereas it is lying at 458 cm^{-1} for both sample 3 and the reference sample. Γ_{Be} for the sample 3 and the reference sample are close to 8 cm^{-1}, meaning the amount of defects is close for these two samples. For sample 1 and 2, it is higher (14 cm^{-1} for sample 2 and 27 cm^{-1} for sample 1). The logarithmic scale used here allows to distinguish several additional broad bands (413, 544 and 616 cm^{-1}) that were first evidenced in [27], and called defect induced bands. Note that the bands marked by stars are due to the lasers used and are not related to the samples. Indeed Raman spectroscopy does not probe the full Phonon Density Of States (PDOS) but the only modes located at the Gamma point of the Briouillin Zone (BZ). This selection rule is relaxed by defects as defects break the translational symmetry of the crystal. As a consequence, part of the full PDOS is revealed thanks to defects, leading to additional bands in the Raman spectra. The intensity of these bands reaches values as high as 23 % of the Raman active E_{2G} mode height's. These bands are more intense for sample 1 than sample 2, which may be related to high

defect contents. Note that these bands are also present in the commercial reference and sample 3, with both a height close to 1%. As crystal sizes for these 2 samples are respectively several microns and 19 nm, then the presence of these bands is not related directly to the crystal size. We then conclude that it is related to the defect content, defect being a term which can be impurity, vacancy, or other kind of defects.

Changing the wavelength does not change the global shape: the band related to the E_{2G} mode is more downshifted to low frequencies and broader for the sample 1 than for the others. Some differences exist: for example, the height of the PDOS diminishes monotonically with the decrease of the laser wavelength (from 23% with 633 nm down to 4% with 325 nm for the sample 1). σ_{Be} does not display a monotonic evolution with the laser wavelength nor for sample 1 nor for sample 2 or 3. It could be due to the local influence of defects that change the Be-Be frequency by changing the electronic structure and/or the bond length. Dispersion of the band related to the E_{2G} mode is however more surprising for sample 3 than for the others because sample 3 has a low amount of defects and the dispersion is the same order of magnitude than for sample 1 and 2. The reference sample, which has the same amount of defects than sample 3, oppositely, does not disperse in the range 325 - 633 nm. From that we can conclude that the shifts observed for sample 1, 2 and 3 are due to stress [23] in the deposited layer, the non monotonic behavior being caused by two effects: stress gradients existing in the deposited layers and the penetration depth of the laser that is wavelength dependant. This point will be investigated in more details on the implanted samples part.

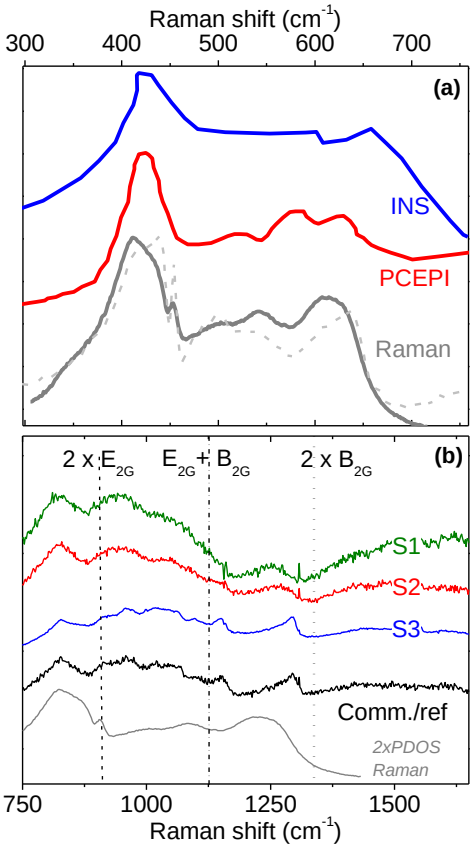

Figure 3. *Be phonon density of states (a) and 2nd harmonic PDOS (b) spectral regions. In (a), the phonon density of states obtained after removing the E_{2G} Raman active mode is compared to the PDOS measured by INS and by PCEPI [48].*

Figure 3-a displays the PDOS of beryllium crystals as measured in the literature [48] by Neutron Scattering (INS) or Point Contact Electron Phonon Coupling Interaction (PCEPI), and compared to two Raman spectra (sample 1 and 2, containing defects). On these Raman spectra, a multiple band fit has been done close to 458 cm^{-1} before the band corresponding to the E_{2G} mode has been subtracted. One can see the good agreement between these spectra and the PDOS, allowing us to claim that these bands are due to the PDOS. We mention that some differences exist between the PDOS of the two samples obtained with Raman spectroscopy, which can be related to different stress existing in the layer, as was also pointed out when describing figure 2. Obtaining quantitative information from that observation is not under the scope of this work but could be the bjective of a next work.

Figure 3-b displays the 750 -1700 cm^{-1} spectral range for sample 1, 2, 3 and the commercial reference sample. This range is of interest for the following reason. Frequencies measured by Raman spectroscopy correspond to the transition of a given oscillator from the vibrational ground state, noted v0, to the first exited one, noted v1. Also a double excitation from v0 to v2 might happen, which is

characterized by twice the frequency from v0 to v1, and is called second harmonic. Because of selection rules, the intensity of such transition is much lower, because of anharmonicity, the corresponding frequency is lower than twice the single excitation frequency. 750 -1700 cm^{-1} is the range where second harmonics are observed for beryllium, it is also the range where Be-D vibrational modes could fall in deuterium containing beryllium samples. In Figure 3b, The wavenumbers of the theoretical second harmonic $2E_{2G}$, $E_{2G}+B_{2G}$ and $2B_{2G}$ modes (vertical lines) together with the second harmonic PDOS have been displayed (multiplying naively by two the wavenumber of the PDOS displayed in Figure 3-a) and compared to the Raman spectra of sample 1, 2, 3 and the commercial reference sample. The broad bands of sample 1 situated at 829, 935, 1043 and 1253 cm^{-1} are very close to the one of the 2PDOS. The relative intensity ratios are slightly different, which can be attributed to anharmonic effects. Phonon calculations based on DFT would be of help for a better understanding, but they are highly time consuming when performed on the full Brillouin Zone on a dense grid of k-points to yield a well-converged PDOS. On both the reference sample and sample 3, which are the one with less disorder, two other narrower bands can be observed at 1151 and 1296 cm^{-1}. They fall close to the $E_{2G}+B_{2G}$ and $2B_{2G}$, falling at +23 and -40 cm^{-1} away from the harmonic wavenumbers, respectively. Note that these bands are not observed for the sample 1 and 2 which display more defects. To resume, these narrow bands are due to a more ordered crystal and the shifts are due to anharmonic effects.

III. 2 Be implanted by D: in depth defect sensitivity

We also studied the influence on the Raman response of ionic implantation on beryllium polycrystals. To tune the amount of defects created under the surface, two impinging ion geometries were used at 2 keV/D: normal incidence (90°) and 45° incidence. Note that the 90° geometry was the one used in our previous study [31], that focused on the formation of beryllium hydride dendrites at high fluences, which is not the scope here. D implantation and vacancy creation profiles were evaluated using the SRIM code[2] [49]. Attenuation of light has been evaluated using the imaginary part of the refractive index, k [50], and deducing the Electromagnetic transmittance $T=\exp(-4\pi ek/\lambda)$ for a given wavelength at a given depth, e. All the information needed to interpret Figure 5 are displayed on Figure 4, which can be resumed as the comparison between penetration of light and ions in function of depth.

[2] This code is widely used to investigate ion-surface interaction phenomena. It is a free access Monte-Carlo computer program based on the binary collision approximation that do not take into account crystal structure or vacancy diffusion (i.e. each single collision event is treated independently between two steps).

Figure 4-a displays the EM transmittance from 244 to 785 nm in beryllium: the higher the wavelength, the deeper light penetrates. We define a useful criteria corresponding to a 90% attenuation energy (corresponding to a transmittance of 10 % at a given depth, for a given wavelength). The left part of the red rectangle on that sub figure represents the zone probed by the 325 nm laser when transmittance is equal to 10%, i.e. from the surface down to 19 nm in depth. The right part of the red rectangle represents the zone probed by the 514 nm laser when transmittance is equal to 10%, i.e. from the surface down to 31 nm in depth. For 488 nm the transmittance reaches 10% at 28 nm in depth. Figure 4-b displays that values for all the wavelengths. The D implantation and vacancy profiles are displayed in figure 4-c and 4-d, respectively. If we believe in SRIM calculations (which gives trends as many mechanisms and effects are not included), we can then estimate that 16 % of the implanted hydrogen atoms are implanted in the range 0-19 nm, 31% in the range 0-28 and 37% in the range 0-31 nm. For the corresponding ranges, the total amount of vacancies created are respectively 37%, 59% and 65 % of the total vacancies created. The lineal density of vacancies is the higher in the range 0-28 nm, being lower by 7.6% in the 0-19 nm range and by 0.4% in the 0-31 nm range.

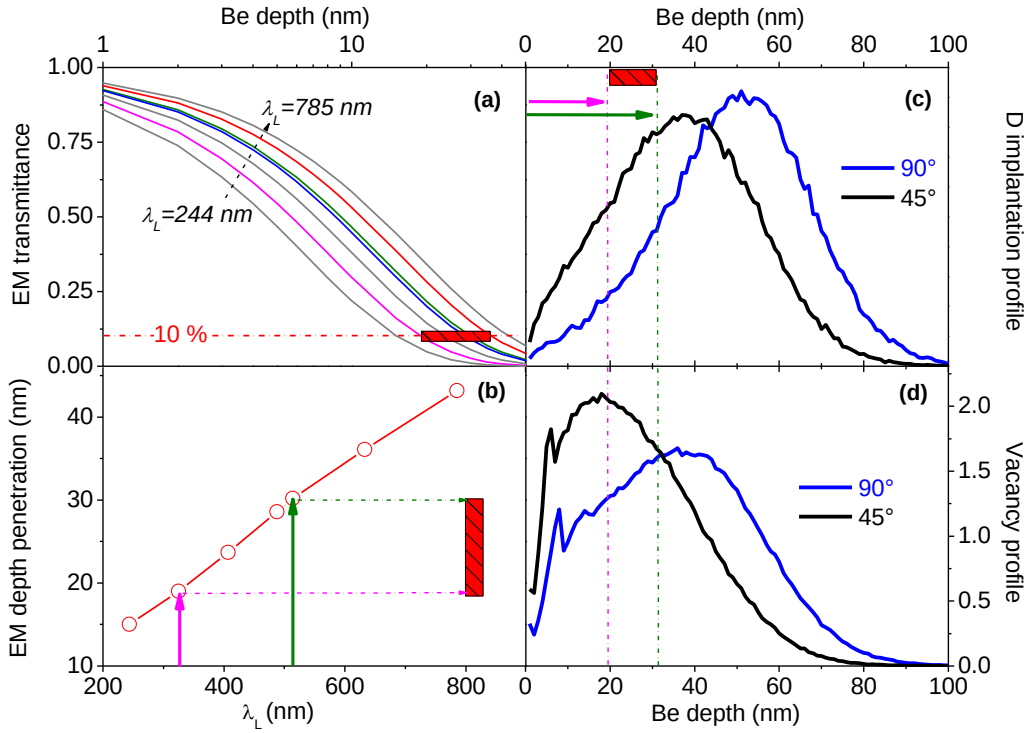

Figure 4. *Comparison of in depth penetration of electromagnetic wave implanted D ions. (a) The transmittance has been plotted for 244, 325, 407, 488, 514, 633 and 785 nm. An arbitrary extinction criterium is defined as when the transmittance equals 10%. (b) This criterium is plotted as a function of the excitation wavelength. (c, d) D implantation and vacancy profiles for two implantation geometries (normal to the surface or at 45° to the surface).*

In figure 5 we compare 514 nm spectra of a pristine Be, a Be sample containing 2 10^{17} D cm^{-2} in the 90° geometry and 325, 488 and 514 nm spectra of Be sample in the 45° geometry. Two main findings can be highlighted given here:

- Lets first focus on the comparison between 45° and 90° geometries, recorded using the 514 nm laser. We see that the Be implanted by D in the 90° geometry displays a Raman spectrum with a E_{2G} mode downshifted by 5 cm^{-1} and with an additional broadening of 6.5 cm^{-1} compared to the pristine sample. The PDOS is present, with a relative height ratio of H_{PDOS}/H_{Be} =3%. If we compare with the Be implanted by D in the 45° geometry, we see that the band corresponding to the E_{2G} mode is downshifted by 5 cm^{-1}, with an additional broadening of 30 cm^{-1} compared to the pristine sample. The PDOS is rising, with a relative height ratio H_{PDOS}/H_{Be} of 24%. The band position is the same in the two implantation geometries. However the band width Γ_{Be} is increased by a factor 2.7 and the PDOS relative height H_{PDOS}/H_{Be} is increased by a factor 11 from the 90° to the 45° geometry. How these differences can be interpreted ? According to SRIMS calculations in the subsurface slab going from 0 down to 31 nm there are more defects (implanted D and vacancy) created in the 45° geometry than in the 90° geometry. Then, it explains why H_{PDOS}/H_{Be} and Γ_{Be} are higher in the first case than in the second.
- Lets now focus on the in depth characterization of the 45° geometry sample using the 325, 488 and 514 nm lasers: on figure 5, σ_{Be}=448 cm^{-1} for 325 nm, σ_{Be}=456 cm^{-1} for 488 nm and σ_{Be}=453 cm^{-1} for 514 nm, which is not evolving monotonically with the laser wavelength. A downshift can be interpreted as a tensile stress in the material, that can be due to defects or impurities [23], here we do not intend to identify the mechanisms precisely but just to give the reader the sensitivity of the technique. Then, we can say that the tensile stress is more pronounced in the first 19 nm below the surface as the 325 nm laser gave the lowest value of σ_{Be}. This tensile stress becomes to be less important in the zone 19-28 nm and increases slightly in the slab 28-31 nm, according to the values of σ_{Be}. What can cause this shift/stress ? Two candidates are the presence of vacancies and implanted deuterium that can create chemical bonds changing the bond lengths [51], [31]. This small change in vacancy concentration can be responsible for the σ_{Be} variation observed using the 3 wavelengths.

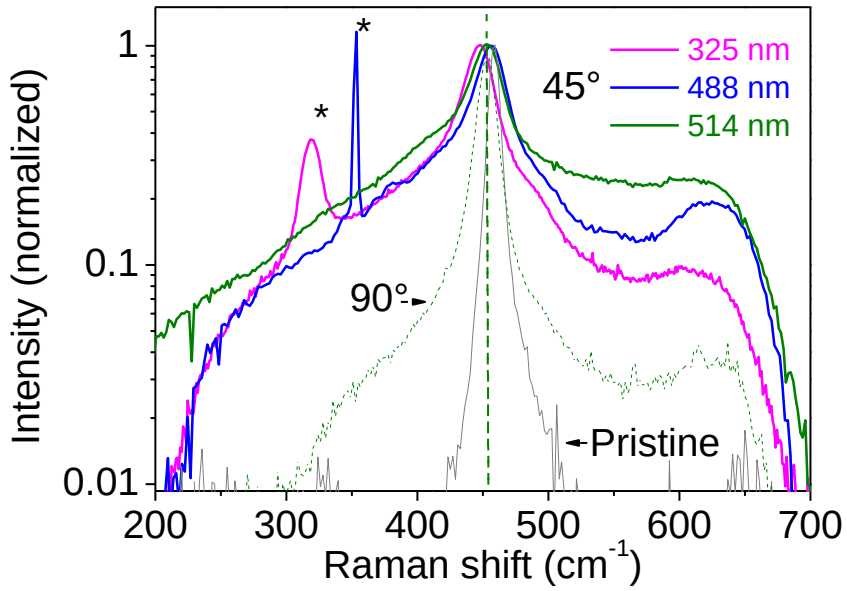

Figure 5. *Normalized Raman spectra of D implanted Be samples. Geometry implantation (90° and 45°) are compared with the 514 nm laser wavelength. The 45° implanted sample is also analyzed with 488 nm and 325 nm lasers.*

III. 3 Be+C codeposits: Be_2C identification

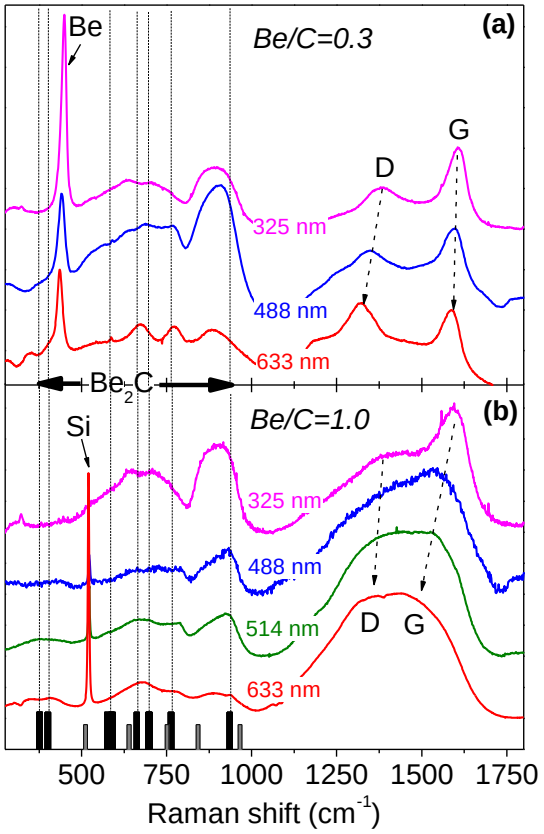

Figure 6. *Multiwavelength Raman spectra of codeposited Be+C samples. (a) The Be/C flux is 0.3. (b) The Be/C flux is 1.0. Calculated vibrational modes are also displayed, for comparison. Bars in black correspond to our calculations, bars in grey correspond to calculations from [52].*

Figure 6 displays the Raman spectra of Be/C co-deposits. Figure 6-a displays the results with a flux Be/C=0.3 ratio whereas Figure 6-b displays the results with a flux Be/C=1. For both, two spectral windows can be distinguished: lower than 1100 cm^{-1} and higher than 1100 cm^{-1}. When the Raman shift is higher than 1100cm^{-1}, two bands, called the D and G bands, are present. These bands are representative of amorphous or nanocrystalline sp^2 carbons. The D band is due to aromatic bonds and the G band to sp^2 stretching bonds. The D band disperses in both Figure 6-a and-b whereas the G band only disperses in Figure 6-b where the bands are broader and overlapped. The interpretation is that the carbon phase is more disordered in Figure 6-b than 6-a, being nanocrystalline in the Figure 6-a and amorphous in the Figure 6-b. More details on information that help in interpreting the spectra can be found in [46, 53].

Below 1100 cm^{-1} three groups of broad overlapped bands are observed at ≈ 895, 675 and 350 cm^{-1} in figure 6-a and b whatever the wavelength used. A narrow band is observed at ≈444 cm^{-1} in figure 6-a and 520 cm^{-1} in figure 6-b. The first narrow band is the E_{2G} mode of Beryllium, but it is

downshifted compared to the bulk beryllium crystal and the second one correspond to the silicon Raman active mode, as shown in Figure 1. The shift of the E_2G mode is stronger using λ_L=633 nm than the other wavelengths, meaning a higher tensile stress exists deeper in the material. The shape of the broad groups of overlapped bands at 895, 675 and 350 cm^{-1} in figure 6-a and b can vary with the wavelength of the laser used, as it will be discussed lower in the text. We calculated by DFT the vibrational spectra at the gamma-point of the Be_2C structure determined in [37, 38]. For comparison with experimental data, the frequencies are displayed in Figure 6 as black histograms, since the respective intensity of each peak has not been determined. One can see that there is a good qualitative agreement between the frequencies obtained by DFT calculations and the measurements that allow us to identify the broad groups of bands at ≈ 895, 675 and 350 cm^{-1} to the Be_2C phase. In more details, calculations predict the existence of modes with frequencies at 376, 400, 575, 587, 590, 662, 697, 699, 762 and 930 cm^{-1} (the complete analysis in terms of symmetry and degeneracy is not under the scope of this paper) that can be qualitatively compared to the overlapped bands measured at: 352, 410, 580, 640, 680, 714, 772, 890, 938 cm^{-1}. Some discrepancy remains: for example few cm^{-1} to ≈20 cm^{-1} shifts exist. This can be due to the fact that DFT calculations were made on a perfect bulk crystal whereas the samples are inhomogeneous and defective (this is confirmed by the full width at half maximum that are important, which is generally the case for an inhomogeneous material). When comparing experience and theory, such differences can usually be expected, too. However one experimental band, lying at 890 cm^{-1}, is not predicted by our DFT calculations. Previous DFT calculations done for Be_2C monolayer that was found to be stable [52], and then that can be called a surface, display modes lying at 511, 639,751, 842 and 966 cm^{-1}. The corresponding frequencies are displayed in grey in Figure 6. All the frequencies corresponding to these modes are close to the frequencies of the bands measured experimentally, and cannot be seen easily because of overlapping, except the mode with the frequency being at 842 cm^{-1}. This mode is not so far from the band lying experimentally at 890 cm^{-1}, that we propose to interpret as being due to a surface effect. Then, our interpretation is that our spectra exhibit a superposition of bulk and surface Be_2C. As the relative intensity ratio of that corresponding bands can vary with the wavelength used, one can conclude that the ratio bulk/surface vary within the depth probed. This leads to the conclusion that the crystallite size of Be_2C diminishes in depth. Obtaining the precise size of the crystallites is not under the scope of this. Also note that the D and G bands are relatively more intense than the Be_2C bands using λ_L=633 nm (compared to the other wavelengths), whereas it is the contrary for the E_2G mode of beryllium. It means that there are more carbons deeper in the material and more Be closer to the surface. An exact calculation of the concentration gradient in the 400 nm layer is, again, not under the scope of this paper but we show here that the information is contained in the data and that Raman microscopy is sensitive to this.

For the experimental conditions of figure 6-b the E_2G mode is not observed as a band but an underlying silicon wafer is visible. The carbon phase is observed but on an amorphous form, and the Be_2C is also observed. Tiny differences can be observed by changing the wavelength and gives a

qualitative information about the relative abundances of the different phases at a given depth. In figure 6-b the underlying silicon wafer gives a lower signature with lower wavelength meaning its signature is extinguished because of the Beer Lamber law, as shown in [54] on another material. As we still see the 520 cm^{-1} band, one can conclude that all the layer is probed by all the lasers used. As we do not see the 520 cm^{-1} silicon band for the sample with Be/C=0.3 (Figure 6-a), the layer absorbs more than for the sample with Be/C=1. This is mainly due to a higher organization in the carbon phase, according to [54] and references therein, and also to the presence in one case of Be crystallites. Then, we cannot prove we probe all the layer in that case.

III.4 Relevant spectroscopic parameters

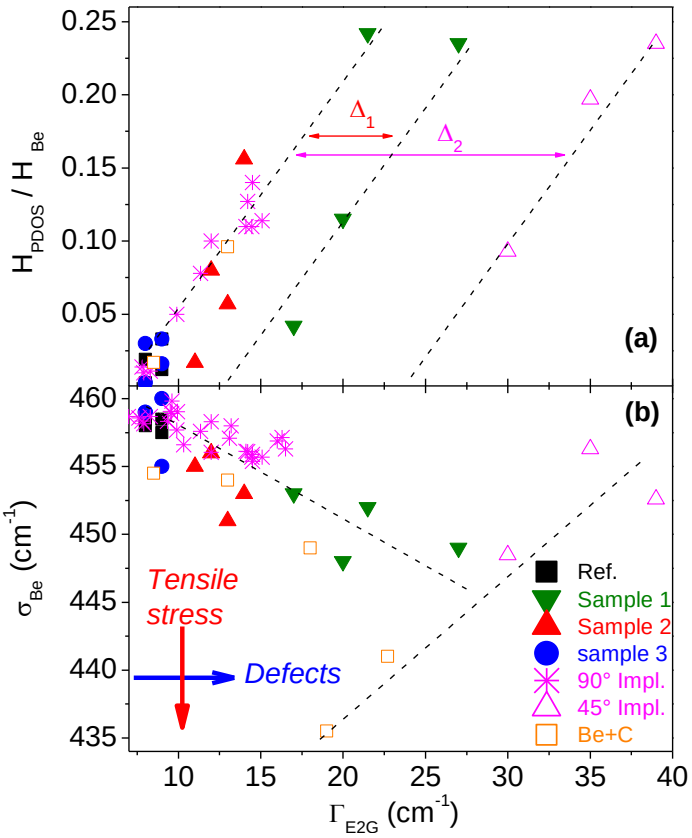

Figure 7. *Raman parameter plots. (a) H_{PDOS}/H_{Be} in function of Γ_{Be}. (b) σ_{Be} in function of Γ_{Be}. All the data were collected from figure 2, 4, and 6 and put all together. Lines are guides for the eyes.*

Figure 7 displays all the relevant spectroscopic parameters of all the samples used, for all the laser wavelengths used, to give general trends that could be used in the future for JET or ITER *post mortem* analysis. We have used the full width at half maximum of the E_2G mode and its intensity comparison with the intensity of the PDOS signatures as a probe for determining the relative amount of defects. The frequency of theE_2G mode is used for probing the stress in the material.

Comparing H_{PDOS}/H_{Be} (the height of the PDOS as measured at 620 cm^{-1} compared to the one of the band related to the E_{2G} mode) and Γ_{Be} in figure 7-a shows that both parameters evolve linearly (when H_{PDOS}/H_{Be} is high, then Γ_{Be} is high) but with some horizontal offset (Δ_1 and Δ_2), varying from zero for the 90° implanted samples up to Δ_2=16 cm^{-1} for the 45° implanted samples. Then, these two spectroscopic parameters do not probe exactly the same kind of defects as the horizontal shifts depend from one sample to the other. The origin of this difference should be studied by complementary disorder-sensitive techniques in the future. Figure 7-b display σ_{Be} in function of $\Gamma_{Be.}$ The natural width, for a defect free crystallite is Γ_{Be} =8cm^{-1}. All the data, whatever the sample, are grouped around two lines: one starting at Γ_{Be} =8cm^{-1} with a negative slope, and one with a positive slope. The one with the negative slope shows that when the amount of defect increases then the tensile stress, which is proportional to the band frequency, also increases. For Γ_{Be} >30 cm^{-1} the slope changes and σ_{Be} increases with Γ_{Be}, leading to a compressive stress. There is an exception which is for beryllium crystallite coexisting with Be_2C and C phases: a downshift of the E_2G band can coexist with a low value of Γ_{Be}. Such a high downshift has been previously observed for photon irradiated BeCW samples in [28]. Understanding this point is not under the scope of this paper but could be understood in the framework of an material oriented study, taking into account coupling between the different phases.

IV. Summary/Discussion:

To resume the main findings: for defective beryllium (deposits or implanted samples), the electric field of the probing laser used to probe the material by means of Raman inelastic scattering penetrates down to 20 nm using 325 nm and down to 30 nm using 514 nm laser, allowing to probe macroscopic gradients (tensile stress, defect concentration,...) . This thickness is typically in the same order of magnitude as the supersaturated layer found in tokamak deposits [12]. We identified defect induced bands that are due to selection rule relaxation caused by defects, giving rise to PDOS and 2PDOS in the range 300-1300 cm^{-1}. These bands lye close to Be-D modes of beryllium hydrides or to Be-O modes of beryllium oxide, which can hinder Be-D and Be-O identification/quantification for

small amounts of D and O. By comparing D-implantation profile obtained by SRIM calculations, the full width at half maximum of the E_2G mode has been shown to be related to the amount of defects, being larger when more defects are created. Horizontal shifts in the plot H_{PDOS}/H_{Be} = f(GBe) may be the finger print of some specific defects affecting the full width at half maximum of the E2G mode of Be. Then, to harness this observation, future efforts should be made varying and controlling systematically the kind and amount of such defects.

To resume the main findings for the Be+C codeposit part:

- Three phases can coexist: Be crystallites, carbon phase (amorphous or nanocrystallite) and Be_2C phase.
- Their relative concentration vary with the in-depth layer
- Be_2C surface and bulk signatures have been identified. We concluded that crystal size changes in depth
- The organization of the carbon phase (amorphous/nanocrystalline) together with the presence of Be crystallitesinfluence the in-depth information retrieved. It leads to a difficulty for estimating the depth probed because of light absorption.

This work was a first step, useful to identify the capabilities of Raman microscopy for studying beryllium based materials. As it concerns the propagation of an electromagnetic field in a medium, many phenomena, that can modify propagation, are involved. It is then difficult to use this technique alone. The interpretation of the multiwavelength Raman microscopy results can be improved in the future by developing multiscale calculations (molecular dynamics) to help interpreting quantitatively band shifts in order to determine precisely the amount of local stress and/or defects in the material, as it was done in silicon of germanene [55, 56]. Using other techniques to control the amount of pollution will also lead to a greater control of the sample and then to the understanding of the underlying mechanisms at play.

V. Conclusion:

In the framework of the ILW JET campaigns, hydrogen isotope content was found higher on the first surface layer, estimated to be a few tens of nm only, and called recently the *supersaturated layer*. It has been suggested that this layer could be composed of beryllium hydrides, without demonstrating it. Unfortunately the actual ion beam techniques are unable to have access to this in depth resolution. In that work, we benchmarked multiwavelength Raman microscopy on laboratory deposited and implanted samples in order to control the capabilities of this technique. We have shown

that on defective beryllium (D-implanted and deposited) we are able to probe ≈ 30 nm. As we are able to detect Be-D bonds, this technique is suitable to be used for the analysis of the *supersaturated layer*. We have also shown that we are able to quantify the amount of defects and to retrieve qualitative information about local stress. By comparing DFT modeling with our results, we were also able to identify Be_2C Raman signatures in Be+C codeposits.

Acknowledgements

This work has been carried out within the framework of the EUROfusion Consortium and has received funding from the Euratom research and training programme 2014-2018 under grant agreement No 633053. The views and opinions expressed herein do not necessarily reflect those of the European Commission. This work has also been carried out thanks to the support of the A*MIDEX project (no ANR-11-IDEX-0001-02) funded by the 'Investissements d'Avenir' French Government program, managed by the French National Research Agency (ANR). C Pardanaud and MI Rusu acknowledge the *Fondation Aix-Marseille Université* for funding the postdoctoral postion. C.P.Lungu, C Porosnicu, P. Dinca, M.Lungu acknowledge the funding by the Romanian National Authority for Scientific Research, UEFISCDI, through project number PN-II-ID-PCE-2011-3-0522.

Bibliography

[1] R. Neu, A.U. Team, E.P. Taskforce, J.E. Contributors, Preparing the scientific basis for an all metal ITER, Plasma Physics and Controlled Fusion, 53 (2011).
[2] V. Philipps, Tungsten as material for plasma-facing components in fusion devices, Journal of Nuclear Materials, 415 (2011) S2-S9.
[3] F. Romanelli, et al., Overview of the JET results with the ITER-like wall, Nuclear Fusion, 53 (2013).
[4] S. Brezinsek, J.-E. Contributors, Plasma-surface interaction in the Be/W environment: Conclusions drawn from the JET-ILW for ITER, Journal of Nuclear Materials, 463 (2015) 11-21.
[5] S. Brezinsek, A. Widdowson, M. Mayer, V. Philipps, P. Baron-Wiechec, J.W. Coenen, K. Heinola, A. Huber, J. Likonen, P. Petersson, M. Rubel, M.F. Stamp, D. Borodin, J.P. Coad, A.G. Carrasco, A. Kirschner, S. Krat, K. Krieger, B. Lipschultz, C. Linsmeier, G.F. Matthews, K. Schmid, J.E.T. Contributors, Beryllium migration in JET ITER-like wall plasmas, Nuclear Fusion, 55 (2015).
[6] J. Roth, E. Tsitrone, A. Loarte, T. Loarer, G. Counsell, R. Neu, V. Philipps, S. Brezinsek, M. Lehnen, P. Coad, C. Grisolia, K. Schmid, K. Krieger, A. Kallenbach, B. Lipschultz, R. Doerner, R. Causey, V. Alimov, W. Shu, O. Ogorodnikova, A. Kirschner, G. Federici, A. Kukushkin, E.P.T. Force, I.P. Team, E. Fusion, D.I.V. Itpa Sol, Recent analysis of key plasma wall interactions issues for ITER, Journal of Nuclear Materials, 390-91 (2009) 1-9.
[7] G.F. Matthews, J.E. Contributors, A.S.-U. Team, Plasma operation with an all metal first-wall: Comparison of an ITER-like wall with a carbon wall in JET, Journal of Nuclear Materials, 438 (2013) S2-S10.
[8] I. Bykov, H. Bergsaker, G. Possnert, Y. Zhou, K. Heinola, J. Pettersson, S. Conroy, J. Likonen, P. Petersson, A. Widdowson, J.E.T. Contributors, Studies of Be migration in the JET tokamak using AMS with Be-10 marker, Nuclear Instruments & Methods in Physics Research Section B-Beam Interactions with Materials and Atoms, 371 (2016) 370-375.
[9] K. Krieger, S. Brezinsek, M. Reinelt, S.W. Lisgo, J.W. Coenen, S. Jachmich, S. Marsen, A. Meigs, G. van Rooij, M. Stamp, O. van Hoey, D. Ivanova, T. Loarer, V. Philipps, J.E.T.E.F.D.A. Contributors,

Beryllium migration and evolution of first wall surface composition in the JET ILW configuration, Journal of Nuclear Materials, 438 (2013) S262-S266.
[10] K. Schmid, M. Reinelt, K. Krieger, An integrated model of impurity migration and wall composition dynamics for tokamaks, Journal of Nuclear Materials, 415 (2011) S284-S288.
[11] J. Likonen, K. Heinola, A. De Backer, S. Koivuranta, A. Hakola, C.F. Ayres, A. Baron-Wiechec, P. Coad, G.F. Matthews, M. Mayer, A. Widdowson, J. Contributors, Deuterium trapping and release in JET ITER-like wall divertor tiles, Physica Scripta, T167 (2016) 014074.
[12] K. Heinola, A. Widdowson, J. Likonen, E. Alves, A. Baron-Wiechec, N. Barradas, S. Brezinsek, N. Catarino, P. Coad, S. Koivuranta, Long-term fuel retention in JET ITER-like wall, Physica Scripta, T167 (2016) 014075.
[13] A. Kallenbach, M. Bernert, R. Dux, L. Casali, T. Eich, L. Giannone, A. Herrmann, R. McDermott, A. Mlynek, H.W. Mueller, F. Reimold, J. Schweinzer, M. Sertoli, G. Tardini, W. Treutterer, E. Viezzer, R. Wenninger, M. Wischmeier, A.U. Team, Impurity seeding for tokamak power exhaust: from present devices via ITER to DEMO, Plasma Physics and Controlled Fusion, 55 (2013).
[14] M. Rubel, P. Petersson, E. Alves, S. Brezinsek, J.P. Coad, K. Heinola, M. Mayer, A. Widdowson, J.E.T. Contributors, The role and application of ion beam analysis for studies of plasma-facing components in controlled fusion devices, Nuclear Instruments & Methods in Physics Research Section B-Beam Interactions with Materials and Atoms, 371 (2016) 4-11.
[15] P. Strom, P. Petersson, M. Rubel, A. Weckmann, S. Brezinsek, A. Kreter, S. Moeller, K. Rozniatowski, Characterisation of surface layers formed on plasma-facing components in controlled fusion devices: Role of heavy ion elastic recoil detection, Vacuum, 122 (2015) 260-267.
[16] M. Reinelt, A. Allouche, M. Oberkofler, C. Linsmeier, Retention mechanisms and binding states of deuterium implanted into beryllium, New Journal of Physics, 11 (2009).
[17] M. Reinelt, C. Linsmeier, Temperature programmed desorption of 1 keV deuterium implanted into clean beryllium, Physica Scripta, T128 (2007) 111-114.
[18] M. Reinelt, C. Linsmeier, Ion implanted deuterium retention and release from clean and oxidized beryllium, Journal of Nuclear Materials, 390-91 (2009) 568-571.
[19] R. Bisson, S. Markelj, O. Mourey, F. Ghiorghiu, K. Achkasov, J.M. Layet, P. Roubin, G. Cartry, C. Grisolia, T. Angot, Dynamic fuel retention in tokamak wall materials: An in situ laboratory study of deuterium release from polycrystalline tungsten at room temperature, Journal of Nuclear Materials, 467 (2015) 432-438.
[20] L. Ferry, (2016).
[21] N. Fernandez, Y. Ferro, D. Kato, Hydrogen diffusion and vacancies formation in tungsten: Density Functional Theory calculations and statistical models, Acta Materialia, 94 (2015) 307-318.
[22] E.A. Hodille, Y. Ferro, N. Fernandez, C.S. Becquart, T. Angot, J.-M. Layet, R. Bisson, C. Grisolia, Study of Hydrogen Isotopes behavior in tungsten by a multi-trapping macroscopic rate equation model, Physica Scripta, T167 (2016) 014011.
[23] G. Gouadec, P. Colomban, Raman spectroscopy of nanomaterials: How spectra relate to disorder, particle size and mechanical properties, Progress in Crystal Growth and Characterization of Materials, 53 (2007) 1-56.
[24] W.J. Evans, M.J. Lipp, H. Cynn, C.S. Yoo, M. Somayazulu, D. Hausermann, G. Shen, V. Prakapenka, X-ray diffraction and Raman studies of beryllium: Static and elastic properties at high pressures, Physical Review B, 72 (2005).
[25] G. Morell, W. Perez, E. ChingPrado, R.S. Katiyar, Anharmonic interactions in beryllium oxide, Physical Review B, 53 (1996) 5388-5395.
[26] M. Boulova, N. Rosman, P. Bouvier, G. Lucazeau, High-pressure Raman study of microcrystalline WO3 tungsten oxide, Journal of Physics-Condensed Matter, 14 (2002) 5849-5863.
[27] C. Pardanaud, M.I. Rusu, G. Giacometti, C. Martin, Y. Addab, P. Roubin, C.P. Lungu, C. Porosnicu, I. Jepu, P. Dinca, M. Lungu, O.G. Pompilian, R. Mateus, E. Alves, M. Rubel, J. contributors, Raman microscopy investigation of beryllium materials, Physica Scripta, T167 (2016) 014027.

[28] L. Avotina, A. Marcu, C. Porosnicu, M. Lungu, A. Stancalie, A.G. Ilie, P.C. Ganea, D. Savastru, J. Kalnacs, C.P. Lungu, G. Kizane, S. Antohe, MULTI-WAVELENGTH LASER IRRADIATION OF Be-C-W COATINGS, Digest Journal of Nanomaterials and Biostructures, 11 (2016) 293-302.
[29] C. Pardanaud, Y. Addab, C. Martin, P. Roubin, B. Pegourié, M. Oberkofler, M. Köppen, T. Dittmar, C. Linsmeier, Raman microscopy as a defect microprobe for hydrogen bonding characterization in materials used in fusion applications, physica status solidi (c), 12 (2015) 98-101.
[30] Y. Addab, C. Martin, C. Pardanaud, J. Khayadjian, K. Achkasov, D. Kogut, G. Cartry, G. Giacometti, M. Cabié, J.L. Gardarein, Formation of thin tungsten oxide layers: characterization and exposure to deuterium, Physica Scripta, T167 (2016) 014036.
[31] C. Pardanaud, M.I. Rusu, C. Martin, G. Giacometti, P. Roubin, Y. Ferro, A. Allouche, M. Oberkofler, M. Köppen, T. Dittmar, C. Linsmeier, Hydrogen retention in beryllium: concentration effect and nanocrystalline growth, Journal of Physics: Condensed Matter, 27 (2015) 475401.
[32] C. Pépin, P. Loubeyre, Layered structure and re-entrant disproportionation observed in crystalline BeH2 under pressure, Physical Review B, 93 (2016) 224104.
[33] C.P. Lungu, C. Porosnicu, I. Jepu, M. Lungu, A. Marcu, C. Luculescu, C. Ticos, A. Marin, C.E.A. Grigorescu, The behavior of W, Be and C layers in interaction with plasma produced by terawatt laser beam pulses, Vacuum, 110 (2014) 207-212.
[34] P. Giannozzi, S. Baroni, N. Bonini, M. Calandra, R. Car, C. Cavazzoni, D. Ceresoli, G.L. Chiarotti, M. Cococcioni, I. Dabo, A. Dal Corso, S. de Gironcoli, S. Fabris, G. Fratesi, R. Gebauer, U. Gerstmann, C. Gougoussis, A. Kokalj, M. Lazzeri, L. Martin-Samos, N. Marzari, F. Mauri, R. Mazzarello, S. Paolini, A. Pasquarello, L. Paulatto, C. Sbraccia, S. Scandolo, G. Sclauzero, A.P. Seitsonen, A. Smogunov, P. Umari, R.M. Wentzcovitch, QUANTUM ESPRESSO: a modular and open-source software project for quantum simulations of materials, Journal of Physics-Condensed Matter, 21 (2009).
[35] J.P. Perdew, GENERALIZED GRADIENT APPROXIMATIONS FOR EXCHANGE AND CORRELATION - A LOOK BACKWARD AND FORWARD, Physica B-Condensed Matter, 172 (1991) 1-6.
[36] D. Vanderbilt, SOFT SELF-CONSISTENT PSEUDOPOTENTIALS IN A GENERALIZED EIGENVALUE FORMALISM, Physical Review B, 41 (1990) 7892-7895.
[37] Y. Ferro, A. Allouche, C. Linsmeier, Absorption and diffusion of beryllium in graphite, beryllium carbide formation investigated by density functional theory, Journal of Applied Physics, 113 (2013).
[38] Y. Ferro, N. Fernandez, A. Allouche, C. Linsmeier, Adsorption of beryllium atoms and clusters both on graphene and in a bilayer of graphite investigated by DFT, Journal of Physics-Condensed Matter, 25 (2013).
[39] C. Pardanaud, C. Martin, P. Roubin, G. Giacometti, C. Hopf, T. Schwarz-Selinger, W. Jacob, Raman spectroscopy investigation of the H content of heated hard amorphous carbon layers, Diamond and Related Materials, 34 (2013) 100-104.
[40] H. Richter, Z.P. Wang, L. Ley, THE ONE PHONON RAMAN-SPECTRUM IN MICROCRYSTALLINE SILICON, Solid State Communications, 39 (1981) 625-629.
[41] C.H. Grein, S. Zollner, M. Cardona, MICROSCOPIC THEORY OF 2ND-ORDER RAMAN-SCATTERING IN SILICON UNDER UNIAXIAL-STRESS, Physical Review B, 43 (1991) 6633-6641.
[42] P. Mishra, K.P. Jain, First- and second-order Raman scattering in nanocrystalline silicon, Physical Review B, 64 (2001).
[43] C. Pardanaud, C. Martin, P. Roubin, G. Giacometti, C. Hopf, T. Schwarz-Selinger, W. Jacob., Raman spectroscopy investigation of the H content of heated hard amorphous carbon layers Diamond Relat. Mater., 34 (2013) 100-104.
[44] S. Reich, C. Thomsen, Raman spectroscopy of graphite, Philosophical Transactions of the Royal Society a-Mathematical Physical and Engineering Sciences, 362 (2004) 2271-2288.
[45] T.W. Scharf, I.L. Singer, Thickness of diamond-like carbon coatings quantified with Raman spectroscopy, Thin Solid Films, 440 (2003) 138-144.
[46] C. Pardanaud, C. Martin, P. Roubin, Multiwavelength Raman spectroscopy analysis of a large sampling ofdisordered carbons extracted from the Tore Supra tokamak, Vib. Spec., 70 (2014) 187-192.

[47] B.W. Mwakikunga, E. Sideras-Haddad, A. Forbes, C. Arendse, Raman spectroscopy of WO3 applications and materials science nano-wires and thermo-chromism study of VO2 belts produced by ultrasonic spray and laser pyrolysis techniques, Physica Status Solidi a-Applications and Materials Science, 205 (2008) 150-154.
[48] A.V. Khotkevich, I.K. Yanson, Atlas of Point Contact Spectra of Electron-Phonon Interactions in Metals, Springer, 1995.
[49] J.F. Ziegler, J.P. Biersack, U. Littmark, The Stopping and Range of Ions in Matter, Pergamon: New York, 1995.
[50] A.D. Rakić, A.B. Djurišic, J.M. Elazar, M.L. Majewski, Optical properties of metallic films for vertical-cavity optoelectronic devices, Appl. Opt., 37 (1998) 5271-5283.
[51] A. Allouche, M. Oberkofler, M. Reinelt, C. Linsmeier, Quantum Modeling of Hydrogen Retention in Beryllium Bulk and Vacancies, Journal of Physical Chemistry C, 114 (2010) 3588-3598.
[52] Y. Li, Y. Liao, Z. Chen, Be2C Monolayer with Quasi-Planar Hexacoordinate Carbons: A Global Minimum Structure, Angewandte Chemie-International Edition, 53 (2014) 7248-7252.
[53] A.C. Ferrari, J. Robertson, Interpretation of Raman spectra of disordered and amorphous carbon, Physical Review B, 61 (2000) 14095-14107.
[54] C. Pardanaud, E. Areou, C. Martin, R. Ruffe, T. Angot, P. Roubin, C. Hopf, T. Schwarz-Selinger, W. Jacob, Raman micro-spectroscopy as a tool to measure the absorption coefficient and the erosion rate of hydrogenated amorphous carbon films heat-treated under hydrogen bombardment, Diamond Relat. Mater., 22 (2012) 92-95.
[55] I. DeWolf, Micro-Raman spectroscopy to study local mechanical stress in silicon integrated circuits, Semiconductor Science and Technology, 11 (1996) 139-154.
[56] C.Y. Peng, C.F. Huang, Y.C. Fu, Y.H. Yang, C.Y. Lai, S.T. Chang, C.W. Liu, Comprehensive study of the Raman shifts of strained silicon and germanium, Journal of Applied Physics, 105 (2009).